

LETTER TO THE EDITOR

# A proto-helium white dwarf with a non-interacting neutron star or black hole companion

## Uncovering the true nature of a candidate hypervelocity B-star

A. Irrgang<sup>1</sup>, S. Geier<sup>2</sup>, U. Heber<sup>1</sup>, T. Kupfer<sup>3</sup>, and S. Bloemen<sup>4</sup>

<sup>1</sup> Dr. Karl Remeis-Observatory & ECAP, Astronomical Institute, Friedrich-Alexander University Erlangen-Nuremberg (FAU), Sternwartstr. 7, 96049 Bamberg, Germany  
e-mail: andreas.irrgang@fau.de

<sup>2</sup> Institut für Physik und Astronomie, Universität Potsdam, Karl-Liebknecht-Str. 24/25, 14476 Potsdam, Germany

<sup>3</sup> Kavli Institute for Theoretical Physics, University of California, Santa Barbara, CA 93106, USA

<sup>4</sup> Department of Astrophysics/IMAPP, Radboud University Nijmegen, P.O. Box 9010, 6500 GL Nijmegen, The Netherlands

Received 26 June 2020 / Accepted 2 July 2020

### ABSTRACT

In the past, SDSS J160429.12+100002.2 was spectroscopically classified as a blue horizontal branch (BHB) star. Assuming a luminosity that is characteristic of BHB stars, the object's radial velocity and proper motions from the second data release of *Gaia* would imply that its Galactic rest-frame velocity exceeds its local escape velocity. Consequently, the object would be considered a hypervelocity star, which would prove particularly interesting because its Galactic trajectory points in our direction. However, based on the spectroscopic analysis of follow-up observations, we show that the object is actually a short-period ( $P = 0.14337069 \pm 0.00000018$  d) single-lined spectroscopic binary system with a visible B-type star (effective temperature,  $T_{\text{eff}} = 15\,840 \pm 160$  K, and surface gravity,  $\log(g) = 4.86 \pm 0.04$ ) that is less luminous than typical BHB stars. Accordingly, the distance of the system is lower than originally thought, which renders its Galactic orbit bound to the Galaxy. Nevertheless, it is still an extreme halo object on a highly retrograde orbit. The abundances of He, C, N, O, Ne, Mg, Al, Si, S, and Ca are subsolar by factors from 3 to more than 100, while Fe is enriched by a factor of about 6. This peculiar chemical composition pattern is most likely caused by atomic diffusion processes. Combining constraints from astrometry, orbital motion, photometry, and spectroscopy, we conclude that the visible component is a stripped star of  $0.25^{+0.15}_{-0.06} M_{\odot}$  that is evolving into a low-mass helium white dwarf. Based on the currently available data, the mass of the unseen compact companion is, with 99% confidence, larger than  $1.5 M_{\odot}$ , that is, it is most likely a neutron star or a black hole. There are very few other systems with similar properties known to date, all of them hosting millisecond pulsars.

**Key words.** binaries: close – binaries: spectroscopic – stars: black holes – stars: individual: SDSS J160429.12+100002.2 – stars: neutron – white dwarfs

### 1. Introduction

The program star SDSS J160429.12+100002.2 is a rather faint ( $G = 17.15$  mag) blue ( $G_{\text{BP}} - G_{\text{RP}} = -0.17$  mag) star of relatively high Galactic latitude ( $b = +41.5$  deg) that was discovered in a search for white dwarf (WD) stars in the tenth data release (DR10) of the Sloan Digital Sky Survey (SDSS, Ahn et al. 2014) by Gentile Fusillo et al. (2015) and Kepler et al. (2015). While the former classify it as a “narrow-line hydrogen star”, that is, a star with a hydrogen-dominated atmosphere but a surface gravity that is lower than those of typical WDs, the latter report a WD spectral type of class DAB star that is flagged as uncertain, with effective temperature,  $T_{\text{eff}} = 23\,819 \pm 270$  K, and surface gravity,  $\log(g) = 5.68 \pm 0.03$ , which is indeed too low for a WD. Because these atmospheric parameters are typical of hot subdwarf stars (sdO/B), Geier et al. (2017) assigned the star to the class of B-type subdwarfs (sdB).

SDSS J160429.12+100002.2 caught our attention because it exhibits a high negative radial velocity ( $-345 \pm 3$  km s<sup>-1</sup>, Geier et al. 2017). Consequently, the object was selected for spectroscopic follow-up observations in an ongoing project that is looking for hot subdwarfs with extreme radial velocities in order

to find high-amplitude radial velocity variables, that is, short-period close binaries (MUCHFUSS, Geier et al. 2015b) as well as high-speed stars unbound to the Galaxy such as the hypervelocity hot subdwarf star US 708 (Hirsch et al. 2005, Geier et al. 2015a). The initial survey, the Hyper-MUCHFUSS project, was restricted to sdO/B stars with radial velocities exceeding  $\pm 100$  km s<sup>-1</sup> (Tillich et al. 2011, Németh et al. 2016, Ziegerer et al. 2017).

Based on the SDSS spectrum, which was the only one available at the time of the aforementioned study, a preliminary spectroscopic analysis was carried out using a grid of synthetic spectra that is based on model atmospheres in local thermodynamic equilibrium (LTE) accounting for metal-line blanketing (Heber et al. 2000). By means of a  $\chi^2$  minimization technique (Napiwotzki et al. 1999), best-fitting atmospheric parameters ( $T_{\text{eff}} = 16\,800 \pm 500$  K,  $\log(g) = 4.72 \pm 0.09$ , and  $\log(n(\text{He})/n(\text{H})) = -2.2$ ) were found that are, on the one hand, considerably different from the ones derived by Kepler et al. (2015) and, on the other hand, consistent with those of blue horizontal branch (BHB) stars in globular clusters (see, e.g., Moni Bidin et al. 2007; Moehler et al. 2011).

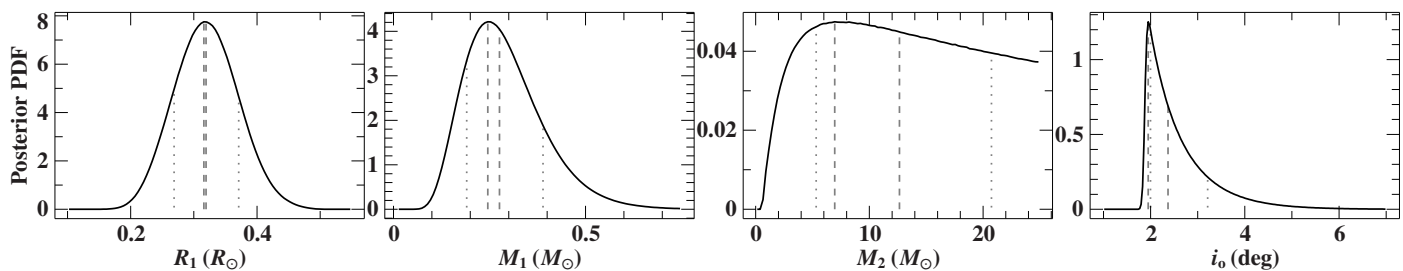


**Fig. 1.** Posterior PDFs for the radius and mass of the visible component ( $R_1$ ,  $M_1$ ), the mass of its unseen compact companion ( $M_2$ ), and the orbital inclination ( $i_0$ ). Maximum and median values as well as  $\pm 1\sigma$  percentiles are marked by dashed and dotted lines, respectively.

Assuming a typical BHB mass of  $0.5 \pm 0.1 M_\odot$ , those preliminary atmospheric parameters gave a spectrophotometric distance  $d = 6.0 \pm 0.9$  kpc that, when combined with the ground-based proper motions available back then, resulted in such a high Galactic rest-frame velocity  $v_{\text{Grf}}$  that the star seemed to be a hypervelocity star, that is, an object that is gravitationally unbound to our Galaxy. This picture did not change when improved proper motions from DR2 of the *Gaia* mission became available later on, which yielded  $v_{\text{Grf}} = 730 \pm 130 \text{ km s}^{-1}$ . Contrary to almost all known hypervelocity stars, the preliminary Galactic orbit of SDSS J160429.12+100002.2 pointed in our direction, which would hint at the origins of the star lying outside of our Galaxy if, indeed, it were to be a BHB star.

In the meantime, high-quality follow-up spectra were taken during the Hyper-MUCHFUSS project. The implications of the analysis of those spectra is presented in the following, where we demonstrate that SDSS J160429.12+100002.2 is not a hypervelocity B-star but a short-period single-lined spectroscopic binary system on a highly retrograde Galactic orbit that hosts the progenitor of a low-mass helium WD and an unseen companion that is most likely a neutron star (NS) or a black hole (BH).

## 2. Analysis

The technical details of the spectroscopic analysis, the investigation of the spectral energy distribution (SED), the light-curve analysis, the modeling of the radial-velocity curve, the kinematic evaluation, and the Bayesian inference method are outlined in Appendix A. We present only the most important results in the main body of the text.

SDSS J160429.12+100002.2 is actually a short-period ( $P = 0.14337069 \pm 0.00000018$  d) single-lined spectroscopic binary system in a low eccentric ( $e = 0.064 \pm 0.027$ ) orbit with a relatively modest velocity semiamplitude ( $K_1 = 38.9 \pm 0.8 \text{ km s}^{-1}$ ). The visible component is a B-type star with effective temperature,  $T_{\text{eff}} = 15\,840 \pm 160$  K, surface gravity,  $\log(g) = 4.86 \pm 0.04$ , and a peculiar abundance pattern that is indicative of ongoing atomic diffusion processes. In terms of number fractions, He and Mg are underabundant by more than 1 dex and Ca by 0.7 dex, while Fe is enriched by about 0.8 dex. Although other chemical species do not exhibit spectral lines in the available optical spectra, upper abundance limits for C, N, O, Ne, Al, Si, S, and Ar can be derived, which are also significantly below solar (from 0.5 dex for N to 2.5 dex for Si), except for Ar where the limit is close to solar. At the level of its precision, the V-band light curve taken in the course of the Catalina Sky Survey (CSS, Drake et al. 2009) shows no indications for photometric variability. The investigation of the SED confirms the spectroscopically derived effective temperature and provides an estimate for the angular diameter  $\Theta = 2R_1/d = (3.82 \pm 0.06) \times 10^{-12}$  ( $R_1$  is the radius of

**Table 1.** Parameters resulting from the Bayesian analysis.

Parameter	Value
Radius $R_1$	$0.32^{+0.06}_{-0.05} R_\odot$
Mass $M_1$	$0.25^{+0.15}_{-0.06} M_\odot$
Mass $M_2$	$7.0^{+13.8}_{-1.7} M_\odot$
Orbital inclination $i_0$	$2.4^{(+0.9)}_{-0.4} \text{ deg}$
Derived parameter	Value
Gravitational redshift $v_{\text{grav}} = GM_1/(R_1 c)$	$0.52^{+0.29}_{-0.16} \text{ km s}^{-1}$
Luminosity $L/L_\odot = (R_1/R_\odot)^2 (T_{\text{eff}}/T_{\text{eff},\odot})^4$	$5.7^{+2.2}_{-1.6}$
Distance $d = 2R_1/\Theta$	$3.74^{+0.65}_{-0.57} \text{ kpc}$

**Notes.** The given numbers are based on the maximum values and the  $\pm 1\sigma$  percentiles of the posterior PDFs shown in Fig. 1. The quantity  $G$  is the gravitational constant,  $c$  is the speed of light. <sup>(a)</sup> Median value of the PDF because the maximum value is not within the  $1\sigma$  interval.

the visible component and  $d$  the distance to the binary system). In addition, it reveals an infrared excess that can be empirically modeled by a blackbody component with a blackbody temperature,  $T_{\text{bb}} = 2300^{+400}_{-600}$  K, and an effective radiation area that is  $16^{+13}_{-5}$  times the projected surface area of the visible star.

Based on Bayesian inference, the radius and mass of the visible component ( $R_1$ ,  $M_1$ ), the mass of the unseen compact companion ( $M_2$ ), and the orbital inclination ( $i_0$ ) can be constrained from the measured angular diameter, *Gaia* DR2 parallax,  $\varpi = 0.127 \pm 0.029 \pm 0.090$  mas (the term  $\pm 0.029$  is the correction for the global parallax offset, see Lindegren et al. 2018), surface gravity, binary mass function, and the condition that  $R_1$  has to be smaller than its respective Roche lobe radius at periastron passage. The properties of the resulting probability distribution functions (PDFs), shown in Fig. 1, as well as the derived stellar parameters are listed in Table 1. The given distance allows us to re-evaluate the kinematic properties of the binary system, which turns out to be on a highly retrograde, halo-like Galactic orbit that is gravitationally bound to the Milky Way.

## 3. Discussion

### 3.1. The nature of the visible component

The analysis of the follow-up spectra yielded improved atmospheric parameters with respect to the preliminary analysis outlined in Sect. 1. The effective temperature turned out to be lower and the surface gravity higher. Figure 2 shows the preliminary and revised position of SDSS J160429.12+100002.2 in the Kiel diagram, demonstrating that the new parameters are no longer consistent with those of a BHB star because they place the star below the zero-age horizontal branch (HB). This conclusion is corroborated by our mass estimate of  $M_1 = 0.25^{+0.15}_{-0.06} M_\odot$ , which

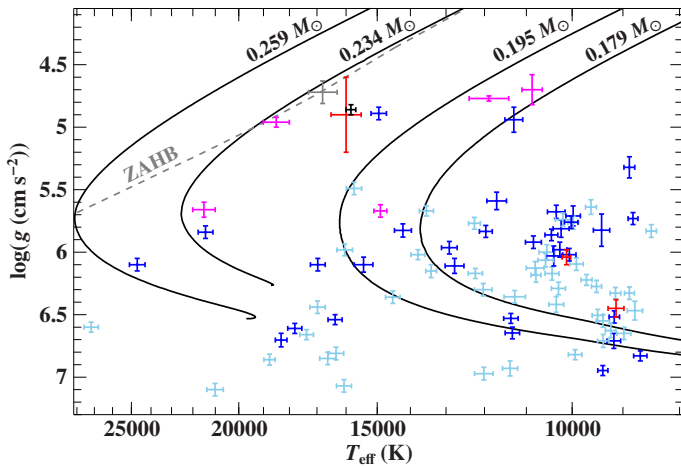


**Fig. 2.** Preliminary and revised position of the program star (gray and black  $1\sigma$  error bars) in the Kiel diagram. The solid lines are tracks for stripped helium cores from Driebe et al. (1998) labeled with their respective masses (stars evolve from top to bottom). For reference, the locus of the zero-age horizontal branch (ZAHB) for  $[\text{Fe}/\text{H}] = -1.48$  (Dorman et al. 1993) is shown as gray dashed line, the 75 ELM binaries from the ELM survey (Brown et al. 2020) in blue (with light blue marking objects that orbit in the Galactic disk according to Brown et al. 2020), the five pre-ELM WDs GALEX 1717+6757, HD 188112, EL CVn, WASP 0247–25 B, and EVR-CB-001 which are mentioned in the text are presented in magenta, and the three systems with millisecond pulsars from Table 2 are in red.

is lower than the typical BHB mass of  $0.5 \pm 0.1 M_{\odot}$ . Instead, the gathered observations suggest that the program star is a proto-helium WD.

The evolutionary histories of BHB stars and helium WDs are very similar. The HB is a sequence of core-helium burning stars that formed after the ignition of helium burning at the tip of the red giant branch (RGB). The morphology of the HB is determined by the mass of the hydrogen envelope, the lower it is, the bluer the HB star appears. Hence, in order to populate the BHB, a considerable fraction of the envelope mass must have been lost during the transition from the RGB to the HB. However, it is conceivable that mass loss occurs even before the progenitor star has reached the tip of the RGB and ignited helium burning in the core. The outcome of such an early mass loss are stripped stars that cool down and become low-mass helium WDs. If they are less massive than  $0.3 M_{\odot}$ , they are called extremely low-mass (ELM) WDs. The high mass loss that is necessary to strip off the envelope and to finally form ELM WD stars is most likely due to binary mass transfer (Driebe et al. 1998, Althaus et al. 2013, Istrate et al. 2016). In fact, most of the ELM WDs are found in short-period double-degenerate systems (see Brown et al. 2020 and references therein).

Although the surface gravity of SDSS J160429.12+100002.2 is currently not high enough to classify it as WD, its low mass and its status as short-period binary system make it a prime candidate for being the progenitor of a low-mass helium WD, very much alike the case of EVR-CB-001 ( $T_{\text{eff}} = 18\,500 \pm 500$  K,  $\log(g) = 4.96 \pm 0.04$ ; Ratzloff et al. 2019). This assumption is strengthened by a comparison of the star’s position in the Kiel diagram (Fig. 2) to evolutionary tracks of stripped helium cores (Driebe et al. 1998), which shows that the inferred atmospheric parameters can be well-recovered by a model for a stripped helium core with a mass of about  $0.215 M_{\odot}$  that is evolving into a

WD. This value is well within the derived  $1\sigma$  confidence interval for  $M_1$  (see Table 1) and, hence, consistent with the observations.

### 3.2. The nature of the unseen component

The companion of the visible B-type star does not exhibit signatures in the optical spectra nor in the SED. Despite this lack of direct hints, the currently available constraints, in particular, the orbital motion of the visible component and the condition that the radius of the B-type star should not exceed its Roche lobe radius (at periastron passage), allow the mass of the unseen companion to be estimated in a statistical fashion (see Appendix A.6). The resulting PDF (see Fig. 1) is very broad, which implies that  $M_2$  is not precisely constrained. Nevertheless, masses lower than  $1.5 M_{\odot}$  can be ruled out with 99% confidence. Such a massive object that is completely outshined by a subluminescent companion and that fits into the very close binary system considered here has to be extremely compact, that is, it must be a NS or a BH. The peculiar kinematic properties of the binary system (see Sect. A.5) could then (at least partly) be explained as the result of a strong supernova kick. While the shape of the PDF, which is similar, albeit mostly broader, than that of BHs in low-mass X-ray binary systems (LMXB; see, e.g., Özel et al. 2010), favors a BH, a NS companion is possible as well. The latter statement may be particularly true when noting that the PDF was derived solely from observations, that is, without considering evolutionary assumptions, which probably prefer lower masses, for instance, owing to the slope of the initial mass function, but also introduce presumption-driven biases that we intentionally aimed to avoid. Contrary to a BH, a NS may be detected by performing X-ray and radio observations in order to search for its blackbody emission and radio pulses, respectively (see, e.g., Kilic et al. 2016).

### 3.3. The evolutionary history and fate of the binary system

Binary systems containing low-mass (proto-)helium WDs in close orbits around NSs have already been observed in systems hosting millisecond pulsars (e.g., Jacoby et al. 2005, Nice et al. 2005, Bassa et al. 2006, Kaplan et al. 2013, Antoniadis et al. 2013, Mata Sánchez et al. 2020) and studied in theory (e.g., Driebe et al. 1998, Althaus et al. 2013, Istrate et al. 2014a, Istrate et al. 2016). According to those models, the progenitor systems are composed of a massive ( $\sim 10\text{--}25 M_{\odot}$ ) primary and a low-mass ( $\sim 1\text{--}2 M_{\odot}$ ) secondary component in a relatively close orbit of a period lasting a few days. Triggered by stellar evolution, the primary expands and, at some point, fills its Roche lobe, which leads to the formation of a common envelope owing to the extreme mass ratio. Despite the accompanying mass loss, the primary remains massive enough to undergo a core-collapse supernova explosion that forms a NS of  $\sim 1.4\text{--}2 M_{\odot}$ . If the spiraled-in close binary system is not disrupted by the supernova explosion, mass transfer via stable Roche lobe overflow occurs when the secondary begins to expand. The absorbed angular momentum of the accreted matter spins up the NS, leading to rotational periods on the order of several milliseconds. This phase, in which the system is a LMXB, continues until the envelope mass of the secondary falls below a critical value, at which the stripping stops because the system detaches again. The resulting binary system has an orbital period of a few hours and consists of a NS plus a stripped helium core that evolves into a low-mass ( $\sim 0.15\text{--}0.45 M_{\odot}$ ) WD. Due to the emission of gravitational waves, the system shrinks for several hundred million



**Table 2.** Parameters of low-mass (proto-)helium WDs in short-period ( $P \leq 9$  h) binary systems with massive ( $M_2 \geq 1.5 M_\odot$ ) companions.

Object	$T_{\text{eff}}$ (K)	$\log(g)$ (cgs)	$M_1$ ( $M_\odot$ )	$M_2$ ( $M_\odot$ )	$P$ (h)	$i_o$ (deg)	Reference
PSR J1738+0333	$9130 \pm 150$	$6.45 \pm 0.07$	$0.182 \pm 0.016$	$1.47^{+0.07}_{-0.06}$	8.51	$32.6 \pm 1.0$	Antoniadis et al. (2012)
PSR J1816+4510	$16\,000 \pm 500$	$4.9 \pm 0.3$	$\geq 0.193 \pm 0.012$	$\geq 1.84 \pm 0.11$	8.66	unknown	Kaplan et al. (2013)
PSR J0348+0432	$10\,120 \pm 90$	$6.04 \pm 0.06$	$0.172 \pm 0.003$	$2.01 \pm 0.04$	2.46	$40.2 \pm 0.6$	Antoniadis et al. (2013)
SDSS J160429.12+100002.2	$15\,840 \pm 160$	$4.86 \pm 0.04$	$0.25^{+0.15}_{-0.06}$	$\geq 1.5$	3.44	$2.4^{+0.9}_{-0.4}$	This work

**Notes.** The effective temperature, surface gravity, and mass of the (proto-)helium WD are  $T_{\text{eff}}$ ,  $\log(g)$ , and  $M_1$ . The mass of the compact companion is  $M_2$ . The orbital period and inclination are  $P$  and  $i_o$ , respectively.

years until it eventually becomes an ultra-compact X-ray binary that finally ends as an isolated BH or as a NS with a planet-mass WD core (see, e.g., Antoniadis et al. 2013).

While those values are at the lower edge of the allowed range given by the derived PDF (see Fig. 1), the masses,  $M_2$ , of the unseen companion of  $\sim 1.5$ – $2 M_\odot$  are likely to be possible for the program star. In that case, SDSS J160429.12+100002.2 would nicely fit into the evolutionary picture outlined in the previous paragraph. On the one hand, the system had to be in the post-LMXB phase because the available optical spectra (see Fig. A.1 for an example) do not exhibit the slightest sign of ongoing mass accretion, which is expected to manifest itself in LMXBs as emission in  $H\alpha$  (see, e.g., Dubus et al. 2004 and references therein). On the other hand, mass transfer could not have ceased too long ago because the radius of the visible component is currently just barely below its Roche lobe radius. This assertion is illustrated in Fig. 3 for a mass of  $0.215 M_\odot$ , which is motivated by evolutionary tracks (see Sect. 3.1), but also valid for higher masses. The signature of a cool extended source observed as infrared excess in the analysis of the SED (see Sect. A.2) may then be caused by circumstellar material formed by the expanding stripped envelope. Compared to most published models, this would imply that Roche lobe overflow detachment occurred quite late.

If the program star hosts a BH instead of a NS, a similar evolutionary history with adjustments to some of the parameter values could be conceivable because the stellar properties of the proto-helium WD do not depend on the mass of its accreting companion (see Istrate et al. 2016 and references therein). Ultimately, tailored binary evolution models are needed to better understand the history of this system.

### 3.4. Similar binary systems

To our knowledge, there are only three other binary systems known that contain a low-mass (proto-)helium WD in a short-period ( $P \leq 9$  h) orbit around a massive ( $M_2 \geq 1.5 M_\odot$ ) compact companion, all of which host millisecond pulsars. Table 2 lists some of their relevant parameters. Those systems are important benchmark objects for stellar binary evolution theory (see, e.g., Istrate et al. 2014b, 2016), which is why this discovery also bears great potential as a test bed for theory. While most properties of the visible component in PSR J1816+4510 are very similar to SDSS J160429.12+100002.2, the orbital period of the former is more than a factor of two longer, which implies that its orbital motion is less extreme. In contrast, the orbital period of PSR J0348+0432 is only three-quarters of that of our program star. The resulting compact orbit and the high mass of the NS have made PSR J0348+0432 a sensitive laboratory for probing gravity in a previously untested strong-field

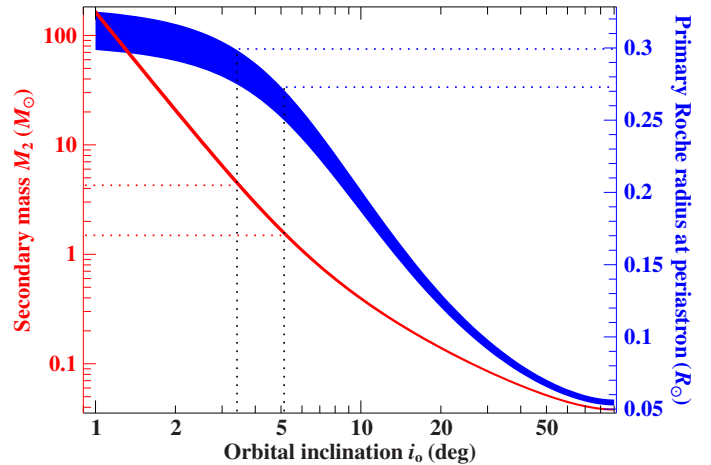


**Fig. 3.** Left ordinate (red): Mass of the unseen companion  $M_2$  as a function of the orbital inclination  $i_o$ : a mass  $M_1 = 0.215 M_\odot$  for the visible component is used to numerically solve the binary mass function given in Eq. (A.3) for  $M_2$ . Right ordinate (blue): Roche radius of the visible component at the pericenter passage based on Eq. (A.6). The widths of both shaded regions cover all involved  $1\sigma$  uncertainties. The range of stellar radii  $R_1$  that follows from  $M_1$  and from the spectroscopically inferred surface gravity  $g = GM_1/R_1^2$  (see Table A.2;  $G$  is the gravitational constant) is indicated by the blue dotted horizontal lines. The other dotted lines mark the limits for the orbital inclination and mass of the unseen companion that arise from the condition that the Roche lobe radius has to exceed the stellar radius.

regime (Antoniadis et al. 2013). Similarly, long-term monitoring of PSR J1738+0333 provided the most stringent constraints at the time for a wide class of gravity theories (Freire et al. 2012). If future radio observations reveal that the program star is orbited by a millisecond pulsar as well, we could expect similar prospects for it.

### 3.5. Abundance studies of (proto-)helium WDs

Regardless of whether SDSS J160429.12+100002.2 contains a pulsar or not, it is one of the few cases that have allowed for a comprehensive abundance analysis of a proto-helium WD. Little information on the chemical composition of other (proto-)helium WDs is currently available, which remains a crucial aspect for the advancement of our understanding of these objects (see, e.g., Istrate et al. 2016). For the companion of the above-mentioned millisecond pulsar PSR J1816+4510, Kaplan et al. (2013) determined super-solar abundances for He, Na, Mg, Si, Ca, and Fe, which, apart from Fe, is completely contrary to what we find here. This is remarkable given that the atmospheric parameters of the two visible components are almost identical. For the

ELM WD SDSS J074511.56+194926.5, Gianninas et al. (2014) measured solar abundances for Mg, Ca, Ti, Cr, and Fe. The most comprehensive abundance studies available are based on ultraviolet spectra of GALEX J1717+6757 (Vennes et al. 2011, Hermes et al. 2014), a pre-ELM WD of similar temperature ( $14\,900 \pm 200$  K) but higher surface gravity ( $5.67 \pm 0.05$  dex) than our program star, and the sdB-type pre-ELM WD HD 188112 ( $T_{\text{eff}} = 21\,500 \pm 500$  K,  $\log(g) = 5.66 \pm 0.06$ ; Heber et al. 2003, Latour et al. 2016). Hermes et al. (2014) derived abundances of C, Al, Si, P, S, Ca, Ti, Cr, and Fe as well as upper limits for N, O, Mg, Sc, and Ni while Latour et al. (2016) determined abundances of Mg, Al, Si, P, S, Ca, Ti, Cr, Mn, Fe, Ni, Zn, Ga, Sn, and Pb as well as upper limits for C, N, and O. The resulting abundance patterns of both objects are most likely produced by atomic diffusion processes. Also, based on ultraviolet spectroscopy, Wang et al. (2020) recently found evidence for atomic diffusion in the atmosphere of the pre-ELM WD EL CVn ( $T_{\text{eff}} = 11\,890 \pm 490$  K,  $\log(g) = 4.77 \pm 0.02$ ), which is the prototype of a class of eclipsing binary systems with pre-ELM WDs and A- or F-type main-sequence companions. Istrate et al. (2017) and Heuser (2018) presented an abundance analysis of the EL CVn-type star WASP 0247–25 B ( $T_{\text{eff}} = 10\,870 \pm 230$  K,  $\log(g) = 4.70 \pm 0.12$ ), which turned out to be somewhat rich in He and deficient in O, Mg, Si, Ca, Ti, and Fe, albeit less pronounced than for SDSS J160429.12+100002.2. Finally, based on a visual inspection of spectra of the ELM survey (Brown et al. 2020), Hermes et al. (2014) concluded that all ELM WDs show Ca in their optical spectra if their surface gravity is lower than  $\log(g) = 5.9$ .

#### 4. Summary and outlook

Based on a comprehensive investigation that utilizes multi-epoch data from astrometry, photometry, and optical spectroscopy, we suggest that SDSS J160429.12+100002.2 is a short-period single-lined spectroscopic binary system containing a low-mass proto-helium WD and a massive compact companion that is most likely a NS or a BH. Only very few other binary systems with similar configurations are known. All of them host millisecond pulsars and are important benchmark objects for stellar binary evolution theory or laboratories for testing gravity under extreme conditions. The derived chemical abundance pattern of the proto-helium WD shows heavy signatures of ongoing atomic diffusion processes and may thus help us to better understand the details of those complex processes, particularly because quantitative abundance studies of proto-helium WDs have been very rare so far. In order to fully exploit the potential of this system as test bed for theory, observations in X-ray, ultraviolet, and radio will eventually be necessary. High-resolution ultraviolet spectroscopy would allow for abundance determinations of many more chemical species than what is currently possible based on optical spectra, while flux measurements in the X-ray and radio regime could help to unravel the nature of the compact companion, for instance, by measuring the blackbody emission or radio pulses of the potential NS companion. Unfortunately, the prospects of extracting constraints from time-series optical photometry are dim given that our estimate for the orbital inclination is very low ( $i_o = 2.4^{+0.9}_{-0.4}$  deg) and that modulations in the light curve are proportional to powers of  $\sin(i_o)$  (see, e.g., Antoniadis et al. 2013). Fortunately, more precise and accurate parallax measurements from future *Gaia* DRs will certainly help to better constrain the stellar parameters of the binary components.

**Acknowledgements.** A.I. and U.H. acknowledge funding by the Deutsche Forschungsgemeinschaft (DFG) through grants IR190/1-1 and HE1356/71-1. S.G.

was supported by the Heisenberg program of the DFG through grants GE 2506/8-1 and GE 2506/9-1. This research was supported in part by the National Science Foundation under Grant No. NSF PHY-1748958. We thank John E. Davis for the development of the SLXFIG module used to prepare the figures in this paper. Based on observations made with ESO Telescopes at the La Silla Paranal Observatory under programme ID 0102.D-0092(A). The William Herschel Telescope is operated on the island of La Palma by the Isaac Newton Group of Telescopes in the Spanish Observatorio del Roque de los Muchachos of the Instituto de Astrofísica de Canarias. The ISIS spectroscopy was obtained as part of W17AN011. Some of the data presented herein were obtained at the W.M. Keck Observatory, which is operated as a scientific partnership among the California Institute of Technology, the University of California and the National Aeronautics and Space Administration. The Observatory was made possible by the generous financial support of the W.M. Keck Foundation. The authors wish to recognize and acknowledge the very significant cultural role and reverence that the summit of Mauna Kea has always had within the indigenous Hawaiian community. We are most fortunate to have the opportunity to conduct observations from this mountain. This work has made use of data from the European Space Agency (ESA) mission *Gaia* (<https://www.cosmos.esa.int/gaia>), processed by the *Gaia* Data Processing and Analysis Consortium (DPAC, <https://www.cosmos.esa.int/web/gaia/dpac/consortium>). Funding for the DPAC has been provided by national institutions, in particular the institutions participating in the *Gaia* Multilateral Agreement. Funding for SDSS-III has been provided by the Alfred P. Sloan Foundation, the Participating Institutions, the National Science Foundation, and the U.S. Department of Energy Office of Science. The SDSS-III web site is <http://www.sdss3.org/>. SDSS-III is managed by the Astrophysical Research Consortium for the Participating Institutions of the SDSS-III Collaboration including the University of Arizona, the Brazilian Participation Group, Brookhaven National Laboratory, Carnegie Mellon University, University of Florida, the French Participation Group, the German Participation Group, Harvard University, the Instituto de Astrofísica de Canarias, the Michigan State/Notre Dame/JINA Participation Group, Johns Hopkins University, Lawrence Berkeley National Laboratory, Max Planck Institute for Astrophysics, Max Planck Institute for Extraterrestrial Physics, New Mexico State University, New York University, Ohio State University, Pennsylvania State University, University of Portsmouth, Princeton University, the Spanish Participation Group, University of Tokyo, University of Utah, Vanderbilt University, University of Virginia, University of Washington, and Yale University. The Pan-STARRS1 Surveys (PS1) have been made possible through contributions of the Institute for Astronomy, the University of Hawaii, the Pan-STARRS Project Office, the Max-Planck Society and its participating institutes, the Max Planck Institute for Astronomy, Heidelberg and the Max Planck Institute for Extraterrestrial Physics, Garching, The Johns Hopkins University, Durham University, the University of Edinburgh, Queen's University Belfast, the Harvard-Smithsonian Center for Astrophysics, the Las Cumbres Observatory Global Telescope Network Incorporated, the National Central University of Taiwan, the Space Telescope Science Institute, the National Aeronautics and Space Administration under Grant No. NNX08AR22G issued through the Planetary Science Division of the NASA Science Mission Directorate, the National Science Foundation under Grant No. AST-1238877, the University of Maryland, and Eotvos Loránd University (ELTE). This publication makes use of data products from the Wide-field Infrared Survey Explorer, which is a joint project of the University of California, Los Angeles, and the Jet Propulsion Laboratory/California Institute of Technology, funded by the National Aeronautics and Space Administration. The CSS survey is funded by the National Aeronautics and Space Administration under Grant No. NNG05GF22G issued through the Science Mission Directorate Near-Earth Objects Observations Program. The CRTS survey is supported by the U.S. National Science Foundation under grants AST-0909182 and AST-1313422.

#### References

- Ahn, C. P., Alexandroff, R., Allende Prieto, C., et al. 2014, *ApJS*, 211, 17
- Alam, S., Albareti, F. D., Allende Prieto, C., et al. 2015, *ApJS*, 219, 12
- Althaus, L. G., Miller Bertolami, M. M., & Córscico, A. H. 2013, *A&A*, 557, A19
- Antoniadis, J., Freire, P. C. C., Wex, N., et al. 2013, *Science*, 340, 448
- Antoniadis, J., van Kerkwijk, M. H., Koester, D., et al. 2012, *MNRAS*, 423, 3316
- Asplund, M., Grevesse, N., Sauval, A. J., & Scott, P. 2009, *Annual Review of Astronomy and Astrophysics*, 47, 481
- Bassa, C. G., van Kerkwijk, M. H., Koester, D., & Verbunt, F. 2006, *A&A*, 456, 295
- Beauchamp, A., Wesemael, F., & Bergeron, P. 1997, *ApJS*, 108, 559
- Bianchi, L., Shiao, B., & Thilker, D. 2017, *VizieR Online Data Catalog*, II/335
- Brown, W. R., Kilic, M., Kosakowski, A., et al. 2020, *ApJ*, 889, 49
- Butler, K. & Giddings, J. R. 1985, in *Newsletter of Analysis of Astronomical Spectra*, No. 9 (Univ. London)

- Chambers, K. C., Magnier, E. A., Metcalfe, N., et al. 2017, *VizieR Online Data Catalog*, 2349
- Dorman, B., Rood, R. T., & O’Connell, R. W. 1993, *ApJ*, 419, 596
- Drake, A. J., Djorgovski, S. G., Mahabal, A., et al. 2009, *ApJ*, 696, 870
- Driebe, T., Schoenberger, D., Bloeker, T., & Herwig, F. 1998, *A&A*, 339, 123
- Dubus, G., Kern, B., Esin, A. A., Rutledge, R. E., & Martin, C. 2004, *MNRAS*, 347, 1217
- Eggleton, P. P. 1983, *ApJ*, 268, 368
- Evans, D. W., Riello, M., De Angeli, F., et al. 2018, *A&A*, 616, A4
- Fitzpatrick, E. L., Massa, D., Gordon, K. D., Bohlin, R., & Clayton, G. C. 2019, *ApJ*, 886, 108
- Freire, P. C. C., Wex, N., Esposito-Farèse, G., et al. 2012, *MNRAS*, 423, 3328
- Fuhrmann, K. 2004, *Astronomische Nachrichten*, 325, 3
- Geier, S., Fürst, F., Ziegerer, E., et al. 2015a, *Science*, 347, 1126
- Geier, S., Kupfer, T., Heber, U., et al. 2015b, *A&A*, 577, A26
- Geier, S., Østensen, R. H., Nemeth, P., et al. 2017, *A&A*, 600, A50
- Gentile Fusillo, N. P., Gänsicke, B. T., & Greiss, S. 2015, *MNRAS*, 448, 2260
- Gianninas, A., Hermes, J. J., Brown, W. R., et al. 2014, *ApJ*, 781, 104
- Giddings, J. R. 1981, PhD thesis, Univ. London
- Heber, U., Edelmann, H., Lisker, T., & Napiwotzki, R. 2003, *A&A*, 411, L477
- Heber, U., Irrgang, A., & Schaffenroth, J. 2018, *Open Astronomy*, 27, 35
- Heber, U., Reid, I. N., & Werner, K. 2000, *A&A*, 363, 198
- Hermes, J. J., Gänsicke, B. T., Koester, D., et al. 2014, *MNRAS*, 444, 1674
- Heuser, C. 2018, PhD thesis, Dr. Karl Remeis-Observatory & ECAP, Astronomical Institute, Friedrich-Alexander University Erlangen-Nürnberg, Sternwartstr. 7, D-96049 Bamberg, Germany
- Hirsch, H. A., Heber, U., O’Toole, S. J., & Bresolin, F. 2005, *A&A*, 444, L61
- Hubeny, I., Hummer, D. G., & Lanz, T. 1994, *A&A*, 282, 151
- Irrgang, A., Kreuzer, S., Heber, U., & Brown, W. 2018, *A&A*, 615, L5
- Irrgang, A., Przybilla, N., Heber, U., et al. 2014, *A&A*, 565, A63
- Irrgang, A., Wilcox, B., Tucker, E., & Schiefelbein, L. 2013, *A&A*, 549, A137
- Istrate, A. G., Fontaine, G., & Heuser, C. 2017, *ApJ*, 847, 130
- Istrate, A. G., Marchant, P., Tauris, T. M., et al. 2016, *A&A*, 595, A35
- Istrate, A. G., Tauris, T. M., & Langer, N. 2014a, *A&A*, 571, A45
- Istrate, A. G., Tauris, T. M., Langer, N., & Antoniadis, J. 2014b, *A&A*, 571, L3
- Jacoby, B. A., Hotan, A., Bailes, M., Ord, S., & Kulkarni, S. R. 2005, *ApJ*, 629, L113
- Kaplan, D. L., Bhalerao, V. B., van Kerkwijk, M. H., et al. 2013, *ApJ*, 765, 158
- Kepler, S. O., Pelisoli, I., Koester, D., et al. 2015, *MNRAS*, 446, 4078
- Kilic, M., Brown, W. R., Heinke, C. O., et al. 2016, *MNRAS*, 460, 4176
- Kurucz, R. L. 1996, in *Model Atmospheres and Spectrum Synthesis*, ed. S. J. Adelman, F. Kupka, & W. W. Weiss (San Francisco: ASP), 160
- Latour, M., Heber, U., Irrgang, A., et al. 2016, *A&A*, 585, A115
- Lindgren, L. 2018, Re-normalising the astrometric chi-square in Gaia DR2, GAIA-C3-TN-LU-LL-124, [www.rssd.esa.int/doc\\_fetch.php?id=3757412](http://www.rssd.esa.int/doc_fetch.php?id=3757412)
- Lindgren, L., Hernández, J., Bombrun, A., et al. 2018, *A&A*, 616, A2
- Maíz Apellániz, J. & Weiler, M. 2018, *A&A*, 619, A180
- Mata Sánchez, D., Istrate, A. G., van Kerkwijk, M. H., Breton, R. P., & Kaplan, D. L. 2020, *MNRAS*, 494, 4031
- Moehler, S., Dreizler, S., Lanz, T., et al. 2011, *A&A*, 526, A136
- Moni Bidin, C., Moehler, S., Piotto, G., Momany, Y., & Recio-Blanco, A. 2007, *A&A*, 474, 505
- Napiwotzki, R., Green, P. J., & Saffer, R. A. 1999, *ApJ*, 517, 399
- Németh, P., Ziegerer, E., Irrgang, A., et al. 2016, *ApJ*, 821, L13
- Nice, D. J., Splaver, E. M., Stairs, I. H., et al. 2005, *ApJ*, 634, 1242
- Özel, F., Psaltis, D., Narayan, R., & McClintock, J. E. 2010, *ApJ*, 725, 1918
- Ratzloff, J. K., Barlow, B. N., Kupfer, T., et al. 2019, *ApJ*, 883, 51
- Schlaflly, E. F. & Finkbeiner, D. P. 2011, *ApJ*, 737, 103
- Schlaflly, E. F., Meisner, A. M., & Green, G. M. 2019, *ApJS*, 240, 30
- Schlegel, D. J., Finkbeiner, D. P., & Davis, M. 1998, *ApJ*, 500, 525
- Sheinis, A. I., Bolte, M., Epps, H. W., et al. 2002, *PASP*, 114, 851
- Smee, S. A., Gunn, J. E., Uomoto, A., et al. 2013, *AJ*, 146, 32
- Spera, M., Mapelli, M., & Bressan, A. 2015, *MNRAS*, 451, 4086
- Tillich, A., Heber, U., Geier, S., et al. 2011, *A&A*, 527, A137
- Tremblay, P. E. & Bergeron, P. 2009, *ApJ*, 696, 1755
- Vennes, S., Thorstensen, J. R., Kawka, A., et al. 2011, *ApJ*, 737, L16
- Vernet, J., Dekker, H., D’Odorico, S., et al. 2011, *A&A*, 536, A105
- Wang, L., Gies, D. R., Lester, K. V., et al. 2020, *AJ*, 159, 4
- Ziegerer, E., Heber, U., Geier, S., et al. 2017, *A&A*, 601, A58



## Appendix A: Analysis details

### Appendix A.1: Quantitative spectroscopic analysis

Our spectral investigation is based on data from four different instruments. The very first spectrum was taken with the SDSS BOSS spectrograph (Smeed et al. 2013) attached to the 2.5 m telescope at Apache Point Observatory, with another five with the ESI spectrograph (Sheinis et al. 2002) mounted at the Keck II telescope, four with the blue arm of the ISIS spectrograph<sup>1</sup> at the William Herschel Telescope, and six with the X-shooter (Vernet et al. 2011) at the ESO Very Large Telescope. Table A.1 lists the date, exposure time, average signal-to-noise ratio (S/N), and measured radial velocity  $v_{\text{rad}}$  of the individual observations.

Following the analysis strategy outlined in Irrgang et al. (2014), we simultaneously fit all those spectra over their entire spectral range to determine the atmospheric parameters and elemental abundances. The underlying synthetic models are computed using a series of three codes. The structure of the atmosphere is computed in LTE with ATLAS12 (Kurucz 1996). Based on this atmosphere, population numbers in non-LTE are calculated with the DETAIL code (Giddings 1981; Butler & Giddings 1985) which numerically solves the coupled radiative transfer and statistical equilibrium equations. Using the non-LTE occupation numbers from DETAIL and more detailed line-broadening data as input, the emerging spectrum is eventually computed with the SURFACE code (Giddings 1981; Butler & Giddings 1985). Recent updates to all three codes (see Irrgang et al. 2018 for details) with respect to non-LTE effects on the atmospheric structure as well as the implementation of the occupation probability formalism (Hubeny et al. 1994) for hydrogen and new Stark broadening tables for hydrogen (Tremblay & Bergeron 2009) and neutral helium (Beauchamp et al. 1997) are considered as well.

The results of the spectroscopic analysis are summarized in Table A.2. The derived effective temperature  $T_{\text{eff}} = 15\,840 \pm 160$  K shows that the program star is of spectral type B. As exemplified in Fig. A.1, all available spectra do only exhibit spectral lines of H, He, Mg, Ca, and Fe, which is quite uncommon for “normal” B-type stars. For reference, main sequence stars of similar temperature and solar chemical composition also show lines of C, N, O, Ne, Al, Si, S, and Ar. Owing to the absence of spectral features of those elements, we are only able to provide upper limits for the respective abundances. The measured abundances of He, Mg, Ca<sup>2</sup>, and Fe significantly differ from those of the Sun. In terms of number fractions, He and Mg are underabundant by more than 1 dex and Ca by 0.7 dex while Fe is enriched by about 0.8 dex. Upper limits for the abundances of C, N, O, Ne, Al, Si, and S are also significantly below solar (from 0.5 dex for N to 2.5 dex for Si). The only exception from this trend is Ar, for which the upper limit is close to solar. This peculiar abundance pattern clearly hints at ongoing diffusion processes. The inferred value for the microturbulence,  $\xi = 2.0^{+1.3}_{-1.5}$  km s<sup>-1</sup>, is rather inconspicuous. In contrast, the radial velocity  $v_{\text{rad}}$  turns out to be variable on a timescale of hours, see Table A.1. Consequently and as discussed in Sect. A.4, our value for the projected rotational velocity  $v \sin(i) = 18.4^{+2.2}_{-2.0}$  km s<sup>-1</sup> is overestimated due to the effect of orbital smearing.

**Table A.1.** List of observations.

Date (d)	Exp. (s)	S/N	Spectrograph	$v_{\text{rad}}^{(a)}$ (km s <sup>-1</sup> )
5706.8079	6306	36	BOSS (2000)	$-320.6 \pm 2.6^{(b)}$
7579.8213	1800	43	ESI (5200)	$-383.8 \pm 1.3$
7579.8427	1800	12	ESI (5200)	$-370.5 \pm 3.1$
7579.8654	1800	47	ESI (8000)	$-343.3 \pm 1.1$
7959.3798	900	35	blue arm ISIS (2.0 Å)	$-313.2 \pm 11.2^{(c)}$
7959.3908	900	38	blue arm ISIS (2.0 Å)	$-308.0 \pm 11.1^{(c)}$
7961.4907	1800	34	blue arm ISIS (1.2 Å)	$-378.6 \pm 10.6^{(c)}$
7961.5132	1800	27	blue arm ISIS (1.2 Å)	$-323.5 \pm 10.8^{(c)}$
8255.0640	1500	62	ESI (8000)	$-349.5 \pm 4.0^{(d)}$
8255.0821	1500	60	ESI (8000)	$-373.3 \pm 3.0^{(d)}$
8564.7278	1800	21	X-shooter UVB (9800)	$-325.2 \pm 1.2$
8564.7278	1800	13	X-shooter VIS (11000)	$-320.5 \pm 2.0$
8565.7407	1800	32	X-shooter UVB (9800)	$-337.5 \pm 0.9$
8565.7408	1800	16	X-shooter VIS (11000)	$-338.6 \pm 1.7$
8565.7668	1800	39	X-shooter UVB (9800)	$-375.8 \pm 0.7$
8565.7669	1800	18	X-shooter VIS (11000)	$-375.9 \pm 1.8$
8565.8164	1800	35	X-shooter UVB (9800)	$-357.4 \pm 0.8$
8565.8165	1800	18	X-shooter VIS (11000)	$-363.6 \pm 1.8$
8565.8427	1800	40	X-shooter UVB (9800)	$-316.5 \pm 0.7$
8565.8428	1800	20	X-shooter VIS (11000)	$-319.3 \pm 1.4$
8565.8693	1800	40	X-shooter UVB (9800)	$-317.0 \pm 0.7$
8565.8693	1800	21	X-shooter VIS (11000)	$-321.9 \pm 1.6$

**Notes.** The first column is the heliocentric Julian date (HJD) at the middle of the observation minus 2 450 000, the second the exposure time, the third the average signal-to-noise ratio (S/N), the fourth the spectrograph with its approximate resolving power  $\lambda/\Delta\lambda$  or  $\Delta\lambda$  in brackets, and the fifth the measured heliocentric radial velocity with statistical  $1\sigma$  uncertainties. <sup>(a)</sup> Not corrected for gravitational redshift. <sup>(b)</sup> Not used for the analysis of the radial-velocity curve because the exposure time is roughly half the orbital period. <sup>(c)</sup> A generic uncertainty of 10 km s<sup>-1</sup> was added in quadrature to account for possible wavelength shifts caused by instrument flexure. <sup>(d)</sup> Uncertainties were increased to account for a small but measurable offset in the wavelength calibration as indicated by the position of the telluric features.

### Appendix A.2: Analysis of the spectral energy distribution

The SED provides an important constraint to cross-check spectroscopic results and to obtain a more comprehensive picture of the program star. For this particular object, photometric measurements covering the ultraviolet, optical, and infrared are available. In order to validate our spectroscopic results, we fitted the observed SED with synthetic SEDs computed with ATLAS12. Because the surface gravity, microturbulence, He abundance, and metallicity are, if at all, only poorly constrained by photometry, they were set to the values determined from spectroscopy (see Table A.2) using Fe as a proxy for metallicity. Consequently, the three quantities  $T_{\text{eff}}$ ,  $\Theta$ , and  $E(44 - 55)$  remained as free parameters to match the observed SED. The angular diameter  $\Theta = 2R_1/d$  ( $R_1$  is the radius and  $d$  the distance of the star, see Heber et al. 2018 for more details) is used as distance scaling factor while the color excess  $E(44 - 55)$  is introduced to account for interstellar reddening, the effect of which is modeled here using the extinction law by Fitzpatrick et al. (2019) with a standard extinction coefficient  $R(55) = 3.02$ . These extinction parameters are analogons of the more widely used color excess  $E(B - V)$  and extinction parameter  $R(V)$ , but with measurements in the Johnson  $B$  and  $V$  filters substituted by monochromatic ones at 4400 Å and 5500 Å (see, e.g., Fitzpatrick et al. 2019).

<sup>1</sup> <http://www.ing.iac.es/astronomy/instruments/isis/>

<sup>2</sup> The Ca abundance is based on population numbers in LTE.

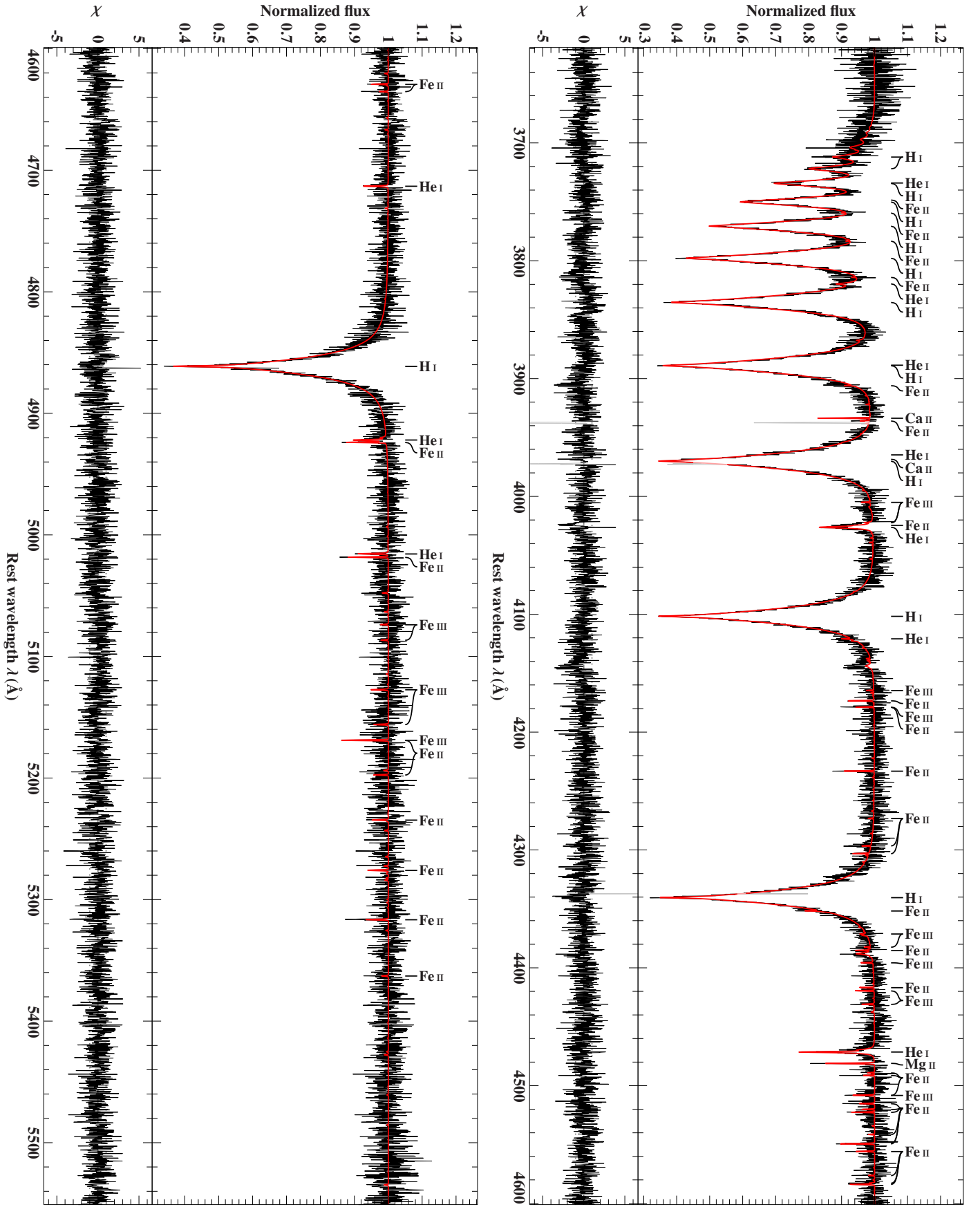


**Fig. A.1.** Exemplary comparison of best-fitting model spectrum (red line) with normalized observation (black line; X-shooter spectrum taken on March 23, 2019, that is, 2458 565.8693 HJD). Light colors mark regions that have been excluded from fitting, e.g., due to the presence of interstellar or telluric lines. Residuals  $\chi$  are shown as well. The optical spectrum only exhibits lines of H, He, Mg, Ca, and Fe.



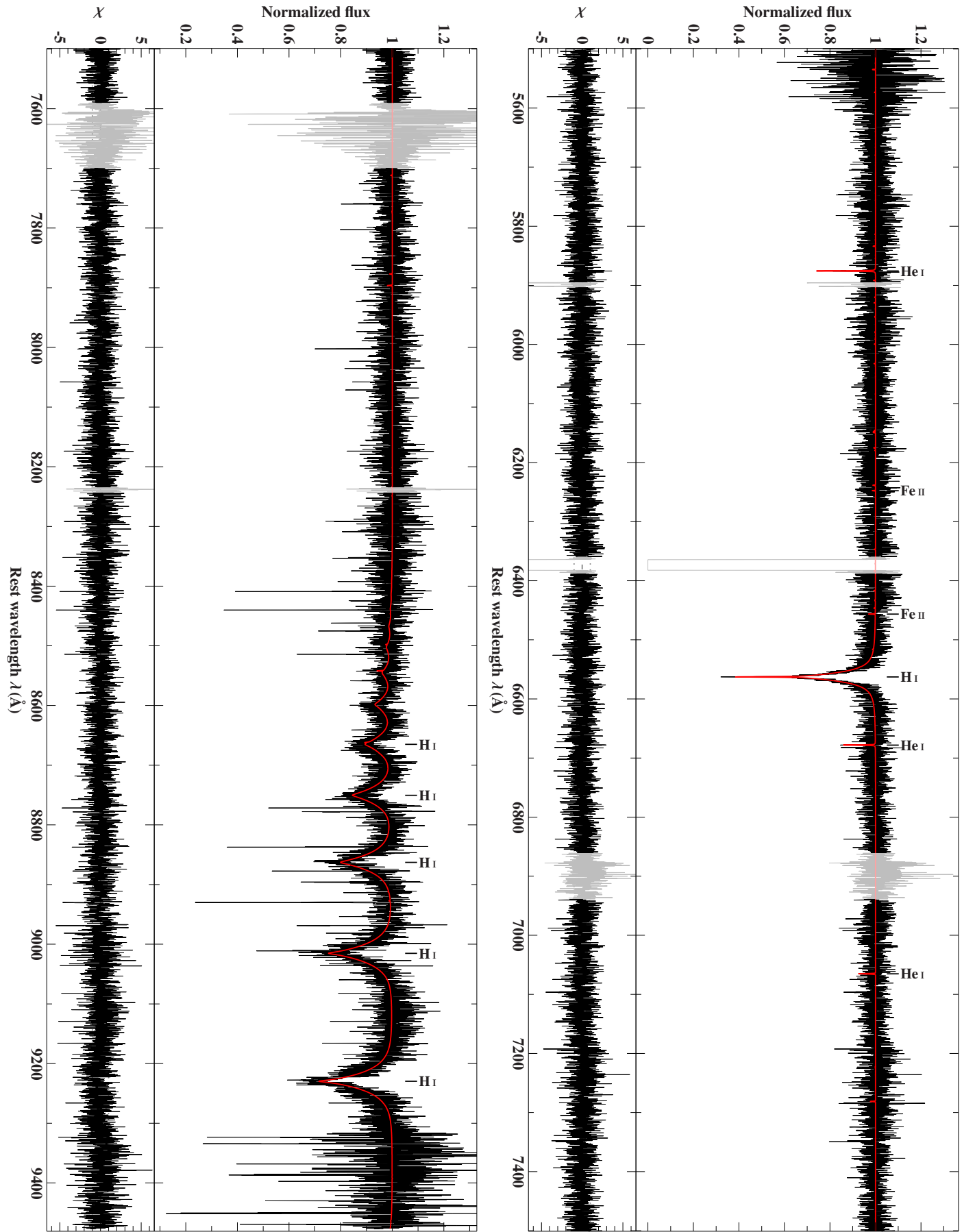


Fig. A.1. continued.

**Table A.2.** Atmospheric parameters and elemental abundances.

	$T_{\text{eff}}$ (K)	$\log(g)$ (cgs)	$v \sin(i)$ (km s <sup>-1</sup> )	$\xi$	$\log(n(x))$											
					He	C	N	O	Ne	Mg	Al	Si	S	Ar	Ca	Fe
Value	15 840	4.86	18.4 <sup>(a)</sup>	2.0	-2.13	-5.66	-4.69	-5.36	-5.97	-5.71	-7.08	-7.00	-6.60	-5.75	-6.38 <sup>(b)</sup>	-3.69
Stat.	+20	+0.01	+0.9	+0.1	+0.02	...	...	...	...	+0.04	...	...	...	...	+0.07	+0.02
Sys.	-20	-0.01	-1.0	-0.1	-0.02	...	...	...	...	-0.04	...	...	...	...	-0.08	-0.02
	+160	+0.04	+2.0	+1.3	+0.04	...	...	...	...	+0.04	...	...	...	...	+0.20	+0.09
	-160	-0.04	-1.7	-1.5	-0.04	...	...	...	...	-0.05	...	...	...	...	-0.22	-0.09
⊙ <sup>(c)</sup>					-1.06	-3.57	-4.17	-3.31	-4.07	-4.40	-5.55	-4.49	-4.88	-5.60	-5.66	-4.50
Value					-1.54	-4.60	-3.57	-4.18	-4.69	-4.34	-5.67	-5.57	-5.11	-4.17	-4.80 <sup>(b)</sup>	-1.96
Stat.					+0.02	...	...	...	...	+0.04	...	...	...	...	+0.07	+0.02
Sys.					-0.02	...	...	...	...	-0.04	...	...	...	...	-0.08	-0.02
					+0.04	...	...	...	...	+0.04	...	...	...	...	+0.20	+0.09
					-0.04	...	...	...	...	-0.05	...	...	...	...	-0.22	-0.09
⊙ <sup>(c)</sup>					-0.57	-2.60	-3.13	-2.22	-2.87	-3.12	-4.23	-3.15	-3.48	-4.11	-4.17	-2.86

**Notes.** The abundance  $n(x)$  is either given as fractional particle number (*upper four rows*) or mass fraction (*lower four rows*) of species  $x$  with respect to all elements. Statistical uncertainties (“Stat.”) are  $1\sigma$  confidence limits based on  $\chi^2$  statistics. Systematic uncertainties (“Sys.”) cover only the effects induced by additional variations of 1% in  $T_{\text{eff}}$  and 0.04 in  $\log(g)$  and are formally taken to be  $1\sigma$  confidence limits (see [Irrgang et al. 2014](#) for details). Abundances without uncertainties are upper limits because the respective chemical elements do not exhibit spectral lines that are strong enough to be measured. <sup>(a)</sup> Affected by orbital smearing and thus overestimated, see Sect. A.4. <sup>(b)</sup> Abundance based on population numbers computed in LTE. <sup>(c)</sup> Protosolar nebula values from [Asplund et al. \(2009\)](#) as reference.

**Table A.3.** Parameters derived from the analysis of the SED.

Parameter	Value
Angular diameter $\log(\Theta)$ (rad)	$-11.418 \pm 0.006$
Color excess $E(44 - 55)$	$0.055 \pm 0.023$ mag
Extinction parameter $R(55)$ (fixed)	3.02
Effective temperature $T_{\text{eff}}$	$15\,800^{+800}_{-700}$ K
Blackbody temperature $T_{\text{bb}}$	$2300^{+400}_{-600}$ K
Blackbody surface ratio	$16^{+13}_{-5}$

**Notes.** The given uncertainties are single-parameter  $1\sigma$  confidence intervals based on  $\chi^2$  statistics with a reduced  $\chi^2$  at the best fit of 0.47.

for details). In order to empirically account for an apparent infrared excess showing up in the WISE data, we also modeled a blackbody component. This introduced two additional free parameters, namely a temperature and a flux weighting factor that is parameterized as surface ratio relative to the stellar component. The results of the fitting procedure are summarized in Table A.3 and illustrated in Fig. A.2. Effective temperatures from spectroscopy and photometry are basically identical, which corroborates our spectroscopic results. Moreover, the inferred interstellar reddening of  $E(44 - 55) = 0.055 \pm 0.023$  mag is consistent with upper limits from reddening maps ([Schlegel et al. 1998](#):  $E(B - V) = 0.060 \pm 0.002$  mag; [Schlafly & Finkbeiner 2011](#):  $E(B - V) = 0.051 \pm 0.002$  mag). The best-fitting parameters of the blackbody component are able to reproduce the observed infrared excess and hint at the presence of a very cool but relatively extended thermal source. Its effective radiation area is  $16^{+13}_{-5}$  times the projected surface area of the star itself.

### Appendix A.3: Analysis of the light curve

The CSS light curve ([Drake et al. 2009](#)) consists of 379 V-band measurements spread over 3101 days. The mean magnitude of this data set is  $17.11 \pm 0.01$  mag and the respective standard deviation is 0.08 mag. The latter is very close to the mean of the stated uncertainties on the individual measurements of 0.09 mag and, thus, expected for a constant source. Nevertheless, we checked whether there are indications for photometric variability on timescales similar to the orbital period (see Sect. A.4) by fitting the light curve with a simple cosine function of the

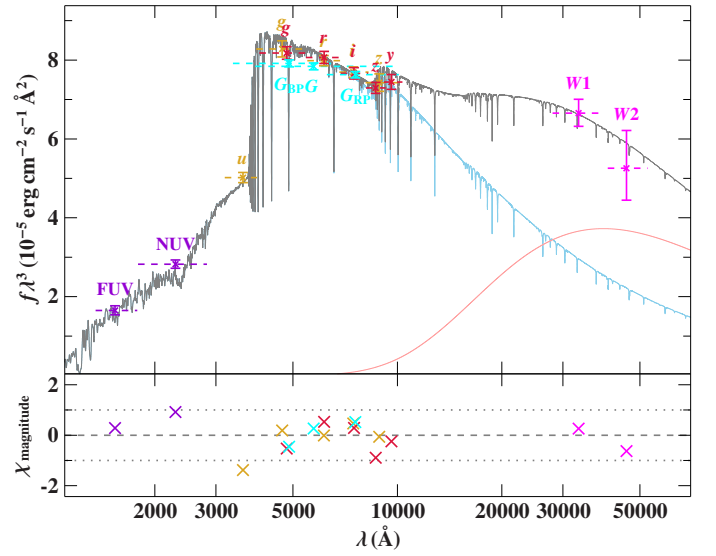


**Fig. A.2.** Comparison of synthetic and observed photometry: The *top panel* shows the SED. The colored data points are filter-averaged fluxes which were converted from observed magnitudes (the respective full width at tenth maximum of the filters are indicated by the dashed horizontal lines), while the gray solid line represents the best-fitting model, i.e., it is based on the parameters from Table A.3, degraded to a spectral resolution of 6 Å. The flux is multiplied with the wavelength to the power of three to reduce the steep slope of the SED on such a wide wavelength range. The individual contributions of the stellar (light blue) and blackbody (light red) component are shown as well. The panel at the *bottom* shows the residuals  $\chi$ , that is, the difference between synthetic and observed magnitudes divided by the corresponding uncertainties. The photometric systems have the following color code: GALEX (violet; [Bianchi et al. 2017](#)); SDSS (golden; [Alam et al. 2015](#)); Pan-STARRS1 (red; [Chambers et al. 2017](#)); *Gaia* (cyan; [Evans et al. 2018](#) with corrections and calibrations from [Maíz Apellániz & Weiler 2018](#)); WISE (magenta; [Schlafly et al. 2019](#)).

form

$$V_{\text{CSS}}(t) = V_{\text{CSS}} + A_{\text{CSS}} \cos(2\pi[(t - T_{\text{ref}})/P + \phi_{\text{ref}}]) \quad (\text{A.1})$$

after removing six obvious ( $> 2\sigma$ ) outliers. The time-dependent magnitude  $V_{\text{CSS}}(t)$  is hence parameterized by a mean magnitude  $V_{\text{CSS}}$ , an oscillation semi-amplitude  $A_{\text{CSS}}$ , and an oscillation frequency  $1/P$ . The parameter  $\phi_{\text{ref}}$  is the phase at the fixed reference

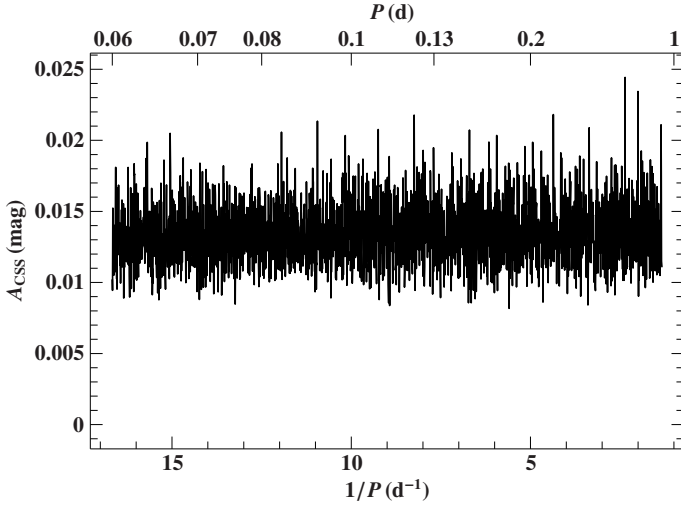


**Fig. A.3.** The oscillation semi-amplitude, which results from fitting the CSS light curve with the cosine model described in Eq. (A.1), as function of the oscillation frequency or period, respectively. The step size in the oscillation frequency was chosen such that phase shifts are always less than 0.02. A maximum filter has been applied to lower the number of points in the plot to a reasonable amount.

epoch  $T_{\text{ref}}$ . Figure A.3 shows the best-fitting semi-amplitude as function of the oscillation frequency. The lack of a distinct maximum implies that – within the level of precision of the CSS light curve – SDSS J160429.12+100002.2 is not photometrically variable.

#### Appendix A.4: Analysis of the radial-velocity curve

Already in the first follow-up observation run in July 2016, variations in the radial velocity became obvious. Within about an hour,  $v_{\text{rad}}$  changed by more than  $40 \text{ km s}^{-1}$ . In a second run in April 2019, enough follow-up observations were collected to construct the radial-velocity curve. For the modeling of this curve, we did not consider the BOSS spectrum because its exposure time is roughly half the orbital period, which might be too long to infer a representative radial velocity.

Given that it is much smaller than the gap between the observation blocks, the determination of the orbital period  $P$  was not trivial. To estimate an upper limit for  $P$ , we looked at the radial-velocity variations in the night at 2458565 HJD (see Table A.1). Within 2.5 h,  $v_{\text{rad}}$  increased from about  $-376 \text{ km s}^{-1}$  to roughly  $-318 \text{ km s}^{-1}$ . This change in  $v_{\text{rad}}$  coincides fairly well with the maximum velocity amplitude inferred from all available observations. For a sinusoidal curve, it would take  $1/2 + N$  times the orbital period to accomplish this maximum change, where  $N \geq 0$  is an integer. Consequently,  $P \approx 2.5 \text{ h} / (1/2 + N) \lesssim 5 \text{ h}$ . To account for the various approximations in this reasoning, we adopted a conservative upper limit of 18 h. A lower limit for  $P$  can be estimated by considering the effect of orbital smearing, that is, spectral lines are smeared out due to the change in radial velocity over the course of an exposure. Assuming that  $v_{\text{rad}}$  increases linearly from its minimum to its maximum value during half the orbital period, it follows that  $(376 - 318) \text{ km s}^{-1} / (P/2)$  times the exposure times of those observations that have sufficient spectral resolution to resolve line broadening (0.42–0.5 h) has to be lower or equal than the measured value for the projected rotational velocity of  $v \sin(i) = 18.4^{+2.2}_{-2.0} \text{ km s}^{-1}$ , which yields  $P \geq 0.42 \text{ h} \times 2 \times 58/20.6 = 2.36 \text{ h}$ .

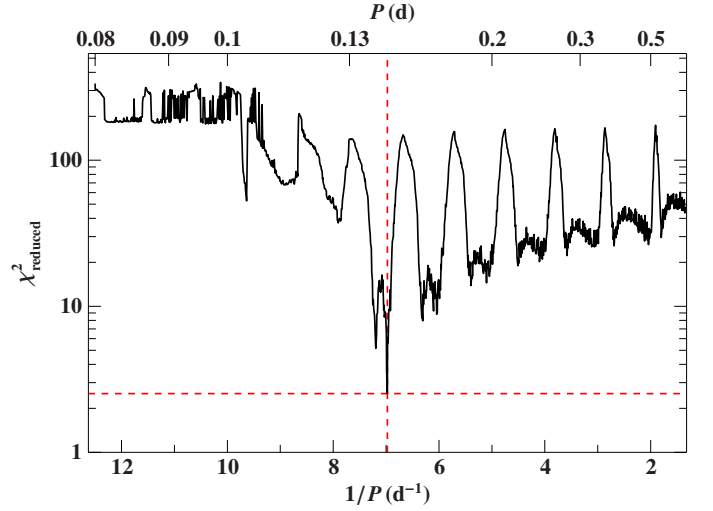


**Fig. A.4.**  $\chi^2$  landscape (“periodogram”), which results from fitting the measured radial velocities with a Keplerian model, as a function of the orbital frequency or period, respectively. The step size in the orbital frequency was chosen such that phase shifts are always less than 0.01. A minimum filter has been applied to lower the number of points in the plot to a reasonable amount. The dashed red lines mark the best fit.

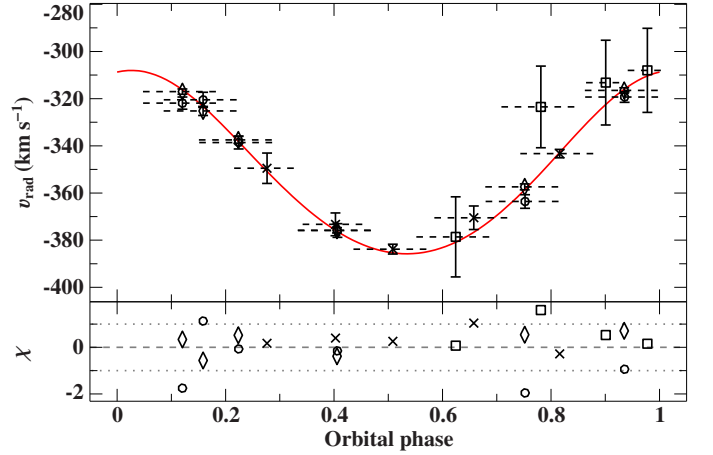


**Fig. A.5.** Phased radial-velocity curve: the measurements are represented by black symbols with  $1\sigma$  error bars while the best-fitting Keplerian model is indicated by the red solid curve. The corresponding orbital parameters are given in Table A.4. ESI spectra are shown as crosses, ISIS spectra as open squares, and X-shooter UVB and VIS spectra as open diamonds and circles, respectively. The dashed horizontal lines indicate the individual exposure times over which the Keplerian curve is averaged before being compared with the measurements. The residuals,  $\chi$ , are shown in the lower panel. An orbital phase of 0 corresponds to the pericenter passage.

Figure A.4 shows the  $\chi^2$  landscape that results from fitting the observed radial velocities with a Keplerian curve for orbital periods between the aforementioned limits. Instead of simply evaluating the Keplerian curve at the midpoint of the exposure times, we average it over the exposure times to account for the fact that the latter are non-negligible fractions of the orbital period. The parameters of the best-fitting configuration with a reduced  $\chi^2$  of about 2.59 are listed in Table A.4 and the corresponding phased radial-velocity curve is shown in Fig. A.5. The star is part of a very close, low-eccentric, short-period single-lined spectroscopic binary system with a large negative systemic radial velocity. The very low values for the mass func-

**Table A.4.** Orbital parameters.

Parameter	Value
Period $P$	$0.14337069 \pm 0.00000018$ d
Epoch of periastron $T_{\text{periastron}}$	$2\,455\,706.037^{+0.008}_{-0.010}$ HJD
Eccentricity $e$	$0.064 \pm 0.027$
Longitude of periastron $\omega$	$349^{+17}_{-26}$ deg
Velocity semiamplitude $K_1$	$38.9 \pm 0.8$ km s $^{-1}$
Systemic velocity $\gamma^{(a)}$	$-349.3 \pm 0.6$ km s $^{-1}$
Derived parameter	Value
Mass function $f$	$(8.7 \pm 0.6) \times 10^{-4} M_{\odot}$
Projected semimajor axis $a_1 \sin(i_o)$	$0.1099 \pm 0.0023 R_{\odot}$
Projected periastron distance $r_p \sin(i_o)$	$0.103 \pm 0.004 R_{\odot}$

**Notes.** The given uncertainties are single-parameter  $1\sigma$  confidence intervals based on  $\chi^2$  statistics. All uncertainties given in Table A.1 have been multiplied with a factor of 1.61 to achieve a reduced  $\chi^2$  of unity at the best fit. <sup>(a)</sup> Not corrected for gravitational redshift.

tion ( $0.00087 \pm 0.00006 M_{\odot}$ ) and the projected semimajor axis ( $0.1099 \pm 0.0023 R_{\odot}$ ) indicate that the orbital inclination  $i_o$  of the system is probably also quite low, that is, we see the system relatively pole-on.

With the inferred orbital parameters from Table A.4, we can now turn the tables and check to what extent our estimate for the projected rotational velocity is actually affected by orbital smearing. Assuming again that  $v_{\text{rad}}$  increases linearly from its minimum to its maximum value during half the orbital period, the amount of orbital smearing can be estimated to be  $4 \times K_1/P \approx 45 \text{ km s}^{-1} \text{ h}^{-1}$  times the relevant exposure times (0.42–0.5 h), which yields values between 19–22 km s $^{-1}$ . Consequently, the measured projected rotational velocity of  $v \sin(i) = 18.4^{+2.2}_{-2.0} \text{ km s}^{-1}$  is heavily affected by orbital smearing and its true value is probably much lower, which implies that the object is a slow rotator or that we see the star’s rotational axis under a very small inclination,  $i$ .

#### Appendix A.5: Kinematic analysis

The unusually large negative systemic radial velocity (see Table A.4) of this binary system calls for a closer inspection of its kinematic properties. Using the spectroscopic distance and the correction for gravitational redshift from Table 1, as well as proper motions from *Gaia* DR2, which seem to be reliable because the “renormalized unit weight error” (RUWE, see Lindegren 2018) indicates a well-behaved astrometric solution (RUWE = 1.01), allows the current position and velocity vector of the system to be computed. Based on the object’s location in the Toomre diagram (Fig. A.6), we conclude that it is on a highly retrograde, halo-like orbit that is more extreme than that of most other known ELM WD binaries. Nevertheless, SDSS J160429.12+100002.2 does no longer qualify as candidate hypervelocity star because its local Galactic escape velocity  $v_{\text{esc}}$  computed in Milky Way mass Model I from Irrgang et al. (2013) significantly exceeds its current Galactic rest-frame velocity  $v_{\text{Grf}} = 430 \pm 90 \text{ km s}^{-1}$ , rendering it undoubtedly bound to the Galaxy ( $v_{\text{Grf}} - v_{\text{esc}} = -200 \pm 90 \text{ km s}^{-1}$ ).

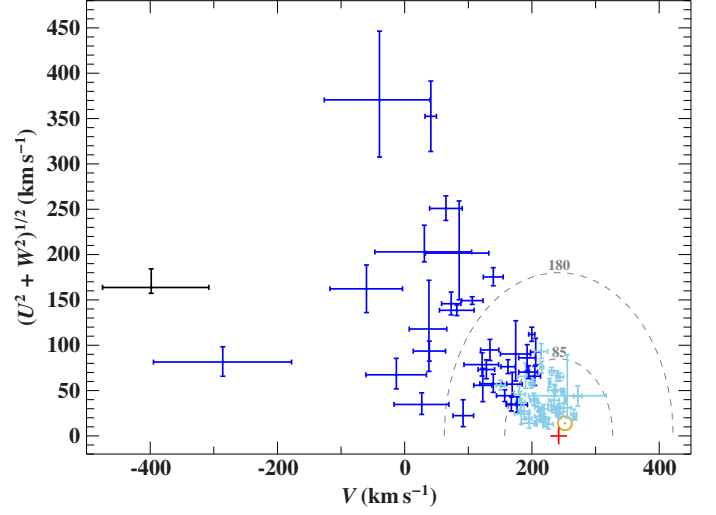


**Fig. A.6.** Position of the program star in the Toomre diagram. The quantity,  $V$ , is the velocity component in direction of Galactic rotation,  $U$ , towards the Galactic center, and  $W$ , perpendicular to the Galactic plane. The star, the Sun, and the local standard of rest (LSR) are marked by a black cross with  $1\sigma$  error bars, a yellow circled dot ( $\odot$ ), and a red plus sign (+), respectively. The meaning of the (light) blue data points is the same as in Fig. 2. The gray dashed circles centered around the LSR represent boundaries for thin (radius of 85 km s $^{-1}$ ) and thick (radius of 180 km s $^{-1}$ ) disk following Fuhrmann (2004).

#### Appendix A.6: Bayesian inference of stellar parameters

The most plausible estimates for the radius and mass of the visible component ( $R_1$ ,  $M_1$ ), the mass of its unseen and thus compact companion ( $M_2$ ), and the orbital inclination ( $i_o$ ) are those that have the highest probability of reproducing the accumulated observational constraints, which are:

1. The value for the surface gravity

$$g(R_1, M_1) = GM_1/R_1^2 \quad (\text{A.2})$$

( $G$  is the gravitational constant) as derived from spectroscopy, see Table A.2.

2. The value for the mass function

$$f(M_1, M_2, i_o) = \frac{M_2 \sin^3(i_o)}{(1 + M_1/M_2)^2} = (1 - e^2)^{3/2} \frac{K_1^3 P}{2\pi G} \quad (\text{A.3})$$

as derived from the analysis of the radial-velocity curve, see Table A.4.

3. The value for the projected periastron distance

$$r_p \sin(i_o) = (1 - e^2)^{1/2} (1 - e) \frac{K_1 P}{2\pi} \quad (\text{A.4})$$

as derived from the analysis of the radial-velocity curve, see Table A.4. In contrast to the surface gravity and the mass function, this quantity cannot be directly computed from a given set of trial parameters  $\{R_1, M_1, M_2, i_o\}$ . Nevertheless, it couples all four parameters via the simple geometric constraint that any star in a binary system has to be smaller than its Roche lobe radius. To account for the slight eccentricity of the binary orbit, we focus in the following on the orbital phase at which the Roche lobe is smallest, that is, on the periastron passage. Using the approximation formula for the relative Roche lobe radius by Eggleton (1983),

$$r_L(M_1, M_2) = \frac{0.49(M_1/M_2)^{2/3}}{0.6(M_1/M_2)^{2/3} + \ln(1 + (M_1/M_2)^{1/3})}, \quad (\text{A.5})$$



the Roche lobe radius at periastron can be written as

$$R_{L,p}(M_1, M_2, i_o) = \frac{r_L(M_1, M_2) r_p \sin(i_o)}{\sin(i_o)}, \quad (\text{A.6})$$

which, combined with the geometric requirement mentioned above, namely  $R_1 \leq R_{L,p}$ , yields

$$h(R_1, M_1, M_2, i_o) := \frac{R_1 \sin(i_o)}{r_L(M_1, M_2)} \leq r_p \sin(i_o). \quad (\text{A.7})$$

Consequently, we wish to determine the probability of having a set of parameters  $\{R_1, M_1, M_2, i_o\}$  given the set of observations  $\{f, g, h\}$ , that is, we have to find an expression for the conditional probability  $P(\{R_1, M_1, M_2, i_o\}|\{f, g, h\})$ . Using Bayes' theorem, we can write

$$P(\{R_1, M_1, M_2, i_o\}|\{f, g, h\}) = CP(\{f, g, h\}|\{R_1, M_1, M_2, i_o\}) \times P(R_1)P(M_1)P(M_2)P(i_o) \quad (\text{A.8})$$

where  $C$  is a normalization constant and  $P(R_1)$ ,  $P(M_1)$ ,  $P(M_2)$ , and  $P(i_o)$  are priors over the values of the four free parameters. To bias the outcome as little as possible, we assume flat priors for  $M_1$  and  $M_2$ , only restricting the latter to values  $\leq 25 M_\odot$  because compact objects with larger masses are highly unlikely in solar-metallicity environments (see, e.g., [Spera et al. 2015](#)):

$$P(M_1) = \text{constant}, \quad (\text{A.9})$$

$$P(M_2) = \begin{cases} \text{constant}, & M_2 \leq 25 M_\odot \\ 0, & M_2 > 25 M_\odot. \end{cases} \quad (\text{A.10})$$

Orbital inclinations are assumed to follow an isotropic distribution:

$$P(i_o) \propto \sin(i_o). \quad (\text{A.11})$$

For the radius,  $R_1$ , we can construct a tailored prior from the measurements of the star's angular diameter ( $\Theta = 3.82 \times 10^{-12}$ ,  $\sigma_\Theta = 0.06 \times 10^{-12}$ , see Sect. A.2) and its *Gaia* DR2 parallax ( $\varpi = 0.127 + 0.029$  mas;  $\sigma_\varpi = 0.090$  mas; the term  $+0.029$  is the global parallax correction advised by [Lindgren et al. 2018](#)). Substituting the inverse distance,  $1/d$ , in the equation for the angular diameter  $\Theta = 2R_1/d$  by the parallax,  $\varpi = 1\text{au}/d$  (au is the astronomical unit), and assuming  $\Theta$  and  $\varpi$  to be distributed Gaussian yields the following integral for the prior probability of  $R_1$ :

$$P(R_1) \propto \iint_0^\infty \exp\left(-\frac{(\Theta - \varpi)^2}{2\sigma_\Theta^2} - \frac{(\varpi - \varpi)^2}{2\sigma_\varpi^2}\right) \delta\left(R_1 - \frac{\Theta \text{au}}{2\varpi}\right) d\Theta d\varpi, \quad (\text{A.12})$$

where  $\delta$  is the Dirac delta function. The resulting distribution, which we obtain by numerical integration, is shown in Fig. A.7. As a final step, by assuming that the three observations  $\{f, g, h\}$  are independent of each other, we can write the likelihood function  $P(\{f, g, h\}|\{R_1, M_1, M_2, i_o\})$  that occurs in Eq. (A.8) as a product of individual probability distributions,

$$P(\{f, g, h\}|\{R_1, M_1, M_2, i_o\}) = \prod_{x \in \{f, g, h\}} P(x|\{R_1, M_1, M_2, i_o\}),$$

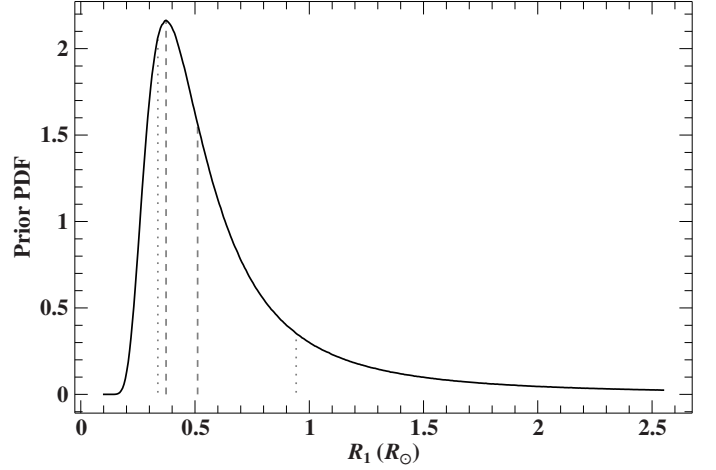


**Fig. A.7.** Prior PDF for the radius of the visible star,  $R_1 = \Theta \text{au}/(2\varpi)$ . The meaning of the dashed and dotted lines is the same as in Fig. 1.

for which we use Gaussian functions with mean value  $\bar{x}$  and standard deviation  $\sigma_x$  as given by the observations:

$$P(x|\{R_1, M_1, M_2, i_o\}) \propto \exp\left(-\frac{(x(R_1, M_1, M_2, i_o) - \bar{x})^2}{2\sigma_x^2}\right) \quad (\text{A.14})$$

$$(\text{A.13})$$

for  $x \in \{f, g\}$  and

$$P(x|\{R_1, M_1, M_2, i_o\}) \propto \begin{cases} 1, & x \leq \bar{x} \\ \exp\left(-\frac{(x(R_1, M_1, M_2, i_o) - \bar{x})^2}{2\sigma_x^2}\right), & x > \bar{x} \end{cases} \quad (\text{A.15})$$

for  $x = h$ . With all expressions in Eq. (A.8) finally defined, it is now possible to compute the posterior PDFs for each of the four parameters by marginalizing out the other three. The result of this exercise is summarized in Table 1 and visualized in Fig. 1. Although small orbital inclinations are in general unlikely owing to Eq. (A.11), the interplay of all observational constraints still favors a very small orbital inclination and, therefore, a high companion mass ( $i_o = 2.4^{+0.9}_{-0.4}$  deg,  $M_2 = 7.0^{+13.8}_{-1.7} M_\odot$ ). The main driver for this is Eq. (A.7), that is, the requirement that the radius of the visible star has to be lower than its Roche radius at periastron passage. To understand this, let us consider an exemplary mass  $M_1 = 0.215 M_\odot$ , which, according to Eq. (A.2) and Table A.2, corresponds to  $R_1 = 0.286 \pm 0.014 R_\odot$ . As demonstrated in Fig. 3, this radius is exceeded by the Roche lobe radius at that given  $M_1$  only for orbital inclinations lower than  $4.2 \pm 1.0$  deg, which, in turn, lead to values for  $M_2$  larger than  $2.5^{+1.8}_{-1.0} M_\odot$ . Because the prior PDF for  $R_1$  (see Fig. A.7) peaks at  $R_1 \approx 0.38 R_\odot$  instead of  $0.286 \pm 0.014 R_\odot$ , even smaller values for  $i_o$  and larger ones for  $M_2$  are mostly needed in order to fit the star into its Roche lobe, finally leading to the values given in Table 1. Interestingly, the posterior PDF for  $R_1$  (see Fig. 1) peaks at about  $0.32 R_\odot$ , that is, it is shifted to lower values with respect to the prior PDF. Because this radius would correspond to a parallax  $\varpi = \Theta \text{au}/(2R_1) = 3.82 \times 10^{-12} \times 1\text{au}/(2 \times 0.32 R_\odot) = 0.26$  mas that is larger than that provided by *Gaia* DR2 ( $\varpi = 0.127 + 0.029 \pm 0.090$  mas), we predict that the parallax in future *Gaia* DRs will be revised upwards.